***Supporting Information***

***for***

# Proton-coupled electroreduction of nitrate on α-$SnWO_4$ and photon-assisted enhancement of ammonia formation

Dikshita Garg,[a] Praveen Kumar,[a] Anubha Rajput,[a] Rupali Gupta[b] and Biswarup Chakraborty*[a]

[a]Department of Chemistry, Indian Institute of Technology Delhi, Hauz Khas, New Delhi – 110016, India

[b]Department of Chemistry, Mahanth Mahadevan Mahila College, Veer Kunwar Singh University, Ara, Bihar – 802301, India

*cbiswarup@chemistry.iitd.ac.in

**Table of Contents**

**Experimental Section.**

**Instrumental details for the material characterizations.**

**Fourier Transform Infrared Spectroscopy (FTIR).** The FTIR measurements were carried out with pallets made by using a sample (~0.1 mg) and KBr powder (~2 mg). The sample and KBr powder were ground in a mortar and pestle properly, and the pellet was prepared by applying hydraulic pressure at a 3-ton pressure. The FTIR measurements were carried out within the 4000-400 $cm^{-1}$ range.

**Raman Spectroscopy.** The Raman spectra were collected using a 532 nm high-resolution laser confocal fiber Raman spectrometer (HORIBA EVOLUTION, HORIBA Jobinyvon, France). The spectra were recorded within the range (200 $cm^{-1}$ to 1600 $cm^{-1}$).

**Powder X-ray diffraction (PXRD).** The PXRD of the samples were collected using a Bruker D8-Advance X-ray diffractometer fitted with CuK ($K_1$ = 1.540598, $K_2$ = 1.544426, K ratio 0.5, $K_{av}$ = 1.541874). The data were recorded with a step size of 3703 and a dwell time of 0.300 s/step within the 10-70° 2θ range.

**Field Emission Scanning electron microscopy (FESEM) and Energy dispersive X-ray spectroscopy (EDX).** The morphology study of the materials was conducted using a TESCAN and a model Magna FESEM instrument. The FESEM-EDX analyses were performed to analyze the morphology and elemental mapping of the materials.

**X-ray electron microscopy (XPS).** The XPS study of the materials was carried out using an ECSA+, Omicron nanotechnology, from Oxford Instrument Germany, equipped with an aluminium monochromator and an aluminium source (Al K radiation hν = 1486.7 eV), and operated at 15 kV voltage and 15 mA current.

**Transmission Electron Microscopy (TEM).** High-resolution transmission electron microscopy (HRTEM) and TEM were performed using a Thermo Fisher Scientific microscope operating at 200 kV to analyse the material. The samples were prepared by drop-casting the material's suspension of 200 μL in acetone on a carbon-coated copper grid (200 mesh, TED PELLA, INC). Before recording data, the TEM grids were allowed to dry at room temperature. The ImageJ software was used for data analysis.

**Contact Angle Measurement.** Contact angle measurements were carried out using a KRÜSS Drop Shape Analyzer DSA100M equipped with manual syringes for customized liquid dispensing. Pellets of pure powder samples were prepared by applying a hydraulic pressure of three tons to obtain a smooth, flat surface. For each measurement, deionized water ($H_2O$) was used as the probe liquid and dispensed in manual syringe mode.

**Brunauer-Emmett-Teller (BET) analysis.** The $N_2$ adsorption-desorption isotherm and pore size distribution measurements were recorded using the Quantachrome instruments NOVA 2000 multi-station nitrogen sorption analyzer standard model version 11.03. The samples were degassed in the cells of the BET instrument at 100 $^oC$ for 12 hr before the analysis.

**UV-Vis diffuse reflectance spectroscopy (DRS).** Diffuse reflectance spectroscopy (DRS) experiments were performed using a UV-2401 Shimadzu spectrophotometer with an

integrating sphere accessory, and $BaSO_4$ was used as a diffuse reflectance standard over 300-800 nm.

**UV-Vis absorption spectroscopy.** The UV-Vis absorption spectra were recorded using Agilent Cary 60 UV-Vis. For each data presented in the manuscript, the baseline was corrected using an in-built module provided by Agilent. All the UV data were collected using Agilent Quartz cells with a total cell volume of 3 mL and path length of 1 cm.

**Electrochemical studies.**

A potentiostat (Gamry Instruments, controlled by Echem Analyst™ Software) was used to study the catalysts' electrochemical activityin a three-electrode setup consisting of Ag/AgCl (aq) as the reference electrode, graphite rod as the counter electrode, and material deposited on carbon cloth as the working electrode. To prepare the working electrode, a carbon cloth sheet was cut into 1 cm × 2 cm dimensions and washed using ultrasonic cleaning with deionized water and acetone. Then, the electrodes were dried in an oven at 45° C. Further, the catalyst's ink was prepared using 3 mg of each catalyst and was uniformly dispersed in ethanol (70 µL) and Nafion solution (30 µL) using the ultrasonic treatment for 30 minutes. The 100 µl of catalyst ink was drop-cast on a 1×1 $cm^2$ area of C cloth.

**Cyclic voltammetry (CV) and linear sweep voltammetry (LSV).** The CV and LSV studies were done in the potential range of 0 to -1.5 V (vs Ag/AgCl) with a scan rate of 10 mV $s^{-1}$. The current density was normalized using the geometrical surface area. The recorded potential was converted to a reversible hydrogen electrode (RHE) by using the following equation:

$$E\ (RHE) = E\ (vs.\ Ag/AgCl) + E^{o}\ (Ag/AgCl) + 0.0591 \times pH \qquad \text{Eq. S1}$$

**Electrochemical nitrate reduction reaction ($eNO_3RR$).** The $eNO_3RR$ was carried out in 20 mL of various electrolytes, and potassium nitrate (0.1 M) served as the source of nitrate. An electrochemical cell containing a three-electrode set-up with a catalyst deposited on carbon cloth as a working electrode, a graphite rod as a counter electrode, and Ag/AgCl (3.5 M KCl aq) as a reference electrode was used. Before each electrochemical run, the electrolyte was purged with argon for 10 minutes to eliminate dissolved oxygen. During the chronoamperometric measurements, the solution was stirred for 1 hour at a rate of 500 rpm. After electrolysis, the concentration of $[NO_2]^-$ and $NH_3$ was detected by the Griess and indophenol blue methods, respectively. Calibration curves, made with standard $[NO_2]^-$ and $NH_3$ solutions, were used for quantification (Figure S8, S9). Also, the charge-transfer coefficient (α) was obtained from the temperature dependence of the Tafel slope according to:

$$\eta = \frac{2.303RT}{\alpha nF} log \frac{j}{j_0} \qquad \text{Eq. S2}$$

**Quantification of ammonia.** The detection and quantification of ammonia were executed using the Indophenol Blue method after electrolysis. At first, the calibration curve was made using $NH_4Cl$ solutions as a standard of different concentrations varying from 0 to 249.34 µM. For the calibration curve, in 5 mL of the $NH_4Cl$ solution of a respective concentration, 2 mL of 10 mg/ mL of phenol solution (in ethanol) was added, followed by the addition of 200 µL

of 0.5 wt% of sodium nitroferricyanide (in water). Later, the pH of the solution was adjusted above 10 using 1 M NaOH. Finally, 100 µL of NaOCl was added to the solution mixture. The resulting solution was incubated for 2 h in the dark, and after that UV-vis spectra were recorded for different concentrations of $NH_4Cl$. The characteristic band at 640 nm was observed for indophenol blue dye. Similarly, produced $NH_3$ was quantified in different electrolytes after chronoamperometry scans at corresponding current densities for 1 h, using the respective electrolyte as analyte.

**Quantification of nitrite.** The detection and quantification of nitrite were executed using the Griess method after electrolysis. Initially, the calibration curve was made using different concentrations of potassium nitrite ($KNO_2$): 0 to 290 µM. Before the calibration curve, sulfanilamide and N-(1-naphthyl) ethylenediamine dihydrochloride (NED) solutions were prepared by dissolving 0.25g of sulfanilamide into 25 mL of a 2.0 M HCl solution, and 20.0 mg of NED in 20.0 mL of deionized water, respectively. Then for the calibration curve, in 5 mL of $KNO_2$ solution of a respective concentration, 100 µL of sulfanilamide, and 100 µL of NED were added. The resulting solution was kept for 30 minutes under standard conditions and after that UV-vis spectra were recorded for different concentrations of $KNO_2$. The characteristic band at 540 nm was observed for diazo dye. Similarly, produced $[NO_2]^-$ was quantified in different electrolytes after chronopotentiometry scans at corresponding current densities for 1 h, using the respective electrolyte as analyte.

**Rotating Disk Electrode (RDE) Experiment**. RDE experiments were performed in acetate buffer (0.2 M, pH 2.8) and 0.1 M $KNO_3$. The electrochemical rate constants ($k$) and kinetic current ($i_k$) were obtained using a Koutecky–Levich (K–L) plot using the following equations:

$$\frac{1}{i_c} = \frac{1}{i_k} + \left[\frac{1}{0.62\, nF\, AD^{2/3}\upsilon^{-1/6}C_0}\right]\omega^{-1/2} \qquad \text{Eq. S3}$$

$$i_k = nFAkc_0 \qquad \text{Eq. S4}$$

where n is the number of transferred electrons for nitrate to ammonia; F is the Faraday constant (96485C $mol^{-1}$); A is the surface area of the electrode (5 mm diameter); D is the diffusion coefficient of $[NO_3]^-$ ($2 \times 10^{-5}$ $cm^2$ $s^{-1}$); $\upsilon$ is the kinematic viscosity (0.0088 $cm^2$ $s^{-1}$); $i_c$ is the current at a defined working potential (V vs RHE); $i_k$ is the kinetic current; $C_0$ is the initial concentration of electrolyte and, k is the electrochemical rate constant. Steady-state voltammograms were recorded at different rotating rates ($\omega$) (rotating rates: 928.57, 1342.9, 1757.1, 2171.4, and 2585.7 rpm) using the cell set-up mentioned above and α-$SnWO_4$ deposited on the working electrode.

**eNO₃RR in tapwater.** The $eNO_3RR$ in tapwater was carried out in 20 mL of acetate buffer (0.2 M, pH = 2.8) prepared in tap water, keeping the other conditions the same. The tapwater was collected from the laboratory in IIT Delhi. The concentration of $[NO_3]^-$ was detected by the previously reported method.[1] Calibration curves, made with standard $[NO_3]^-$, were used for

quantification (Figure S18). In order to check the consistency of nitrate ions present in it, the UV-vis spectra were measured on different days, giving the variation of ±0.01 mg $L^{-1}$.

**Quantification of ammonia by $^1$H Nuclear Magnetic Resonance (NMR).** $^{14}NH_4^+$ were quantified by $^1$H nuclear magnetic resonance (NMR) spectroscopy using 500 MHz JEOL NMR. The samples for NMR were prepared using 300 µL of the electrolyte after the chronopotentiometry experiments. The pH of the electrolyte was adjusted to 3 using 1 M $H_2SO_4$. Further, 100 µL of maleic acid and 100 µL of $D_2O$ were used as internal standard and as solvent.

**Faradaic efficiencies.** The Faradaic efficiencies of $NH_3$ and $[NO_2]^-$ produced through e$NO_3$RR were calculated from the equation below:

$$\text{Faradic Efficiency (\% FE)} = \frac{n \times F \times C \times V}{Q} \times 100 \qquad \text{Eq. S5}$$

where F is the Faradaic constant (96485 C $mol^{-1}$), C is the concentration of $NH_3$/$[NO_2]^-$, V is the electrolyte volume, and Q is the total charge passing the electrode.

**Temperature-dependent $NO_3$RR.** A temperature-dependent electrochemical study was conducted by varying the temperature from 20 to 40 °C. The cell temperature was monitored using a thermometer immersed in the electrolyte, and temperature control was maintained using an oil bath. The activation energy ($E_a$) was determined from the slope of the Arrhenius plot of ln $j_0$ versus 1/T, based on the Arrhenius equation:

$$\frac{d(lnj_0)}{d(\frac{1}{T})} = \frac{E_a}{R} \qquad \text{Eq. S6}$$

where $E_a$ is the activation energy, $R$ is the gas constant, and $T$ is the absolute temperature. where $F$ is the Faraday constant and $n$ is the number of electrons involved in the rate-determining step.

**In-situ IR measurements.** The intermediates and products formed during e$NO_3$RR were monitored using in situ infrared (IR) spectroscopy. Measurements were performed with a Mettler Toledo React IR 700 (SN: C049640472), equipped with a TEMCT detector and a DiComp (diamond) probe connected via a 9.5 mm × 2 m AgX fiber interface. The IR probe was directly immersed in the electrochemical cell, which contained a three-electrode setup: a working electrode (α-$SnWO_4$ loaded on C cloth), a reference electrode (Ag/AgCl in aqueous solution), and a counter electrode (graphite rod). The electrolyte consisted of a 0.2 M acetate buffer (pH 2.8) with 0.1 M $KNO_3$. IR spectra were recorded in real time during chronoamperometric experiments conducted at various applied potentials (-0.05 V to -0.45 V vs RHE), and the solution was stirred at a rate of 500 rpm. All electrochemical measurements were carried out using a CHI 1205C potentiostat.

**In-situ EPR measurements.** EPR spectra of the liquid samples were recorded in a Bruker EPR spectrometer (Biospin, EMXmicro A200) at a room temperature setup. In-situ EPR spectra were collected after 10 minutes of electrolysis at -0.6 V vs. RHE in the presence of DMPO in

both cases: with electrolysis in the absence of nitrate, and with electrolysis in the presence of nitrate.

**Photoelectrocatalytic Nitrate Reduction.** Photoelectrocatalytic (PEC) $NO_3RR$ experiments were carried out in a standard three-electrode PEC cell. The working electrode was prepared by drop-casting 10 µL of catalyst ink (1mg catalyst dispersed in 70 µL ethanol and 30 µL nafion) onto indium tin oxide (ITO) glass (geometric area: 1cm²) and drying at room temperature. A graphite rod was used as a counter electrode, and Ag/AgCl (3.5 N KCl) was used as a reference electrode. The PEC measurements were performed in an acetate buffer (0.2 M, pH 2.8) as electrolyte containing 0.1 M $KNO_3$. Before measurements, the electrolyte was purged with Ar for 10 min to remove dissolved oxygen. Illumination was provided using a 427 nm LED light source at room temperature, placed at a fixed distance of 1 cm from the working electrode.

**Calculation of Incident photon to current efficiency (IPCE):** The IPCE was calculated according to:

$$\text{IPCE} = \frac{1240 \times I_\lambda}{\lambda \times P_\lambda} \qquad \text{Eq. S7}$$

where $I_\lambda$ is the photocurrent in mA $cm^{-2}$, $P_\lambda$ is the light power intensity in mW $cm^{-2}$, and $\lambda$ is the wavelength in nm.

**Table S1.** Comparison of $eNO_3RR$ catalyzed by α-$SnWO_4$ with some reported tungstates and Sn-based electrocatalysts.

| Catalyst | Process | Potential (*vs* RHE) | Electrolyte | $FE_{NH_3}$(%) | Reference |
|---|---|---|---|---|---|
| **α-$SnWO_4$** | $eNO_3RR$ | -0.2 V | 0.2 M AB[#] | 90(±4) | This work |
| **$ZnWO_4$** | $eNO_3RR$ | -0.2 V | 0.2 M AB[#] | 38(±2) | This work |
| **$NiWO_4$** | $eNO_2RR$ | -0.4 V | 0.1 M NaOH | 97.6 | [2] |
| **Ru/$CoWO_4$** | $eNO_3RR$ | -0.7 V | 0.1 M KOH | 95.94 | [3] |
| **$CoWO_4$/CoOOH** | $eNO_3RR$ | -0.276 V | 1 M KOH | 97.54 | [4] |
| **Sn/C** | $eN_2RR$ | -0.4 V | 0.1 M $Na_2SO_4$ | 22.76 | [5] |
| **CoSn-CNF** | $eNO_3RR$ | -0.6 V | 1.0 M KOH | 81.5 | [6] |
| **Ni–Sn alloy** | $eN_2RR$ | -0.4 V | 0.10 M $Na_2SO_4$ | 38.00 | [7] |
| **$Co_3O_4$-$SnO_2$/CC** | $eNO_3RR$ | -0.6 V | 0.1 M NaOH | 98.6 | [8] |
| **Sn-$FeS_2$** | $eNO_3RR$ | -0.5 V | 1 M KOH | 96.7 | [9] |
| **$Fe_xSn_{1-x}S$** | $eNO_3RR$ | -0.3 | 0.1 M AB[#] | 85 | [10] |
| **$Mo_x$@$SnO_2$** | $eNO_3RR$ | -0.2 V | 0.05 M AB[#] | 94 | [11] |

[#]Acetate buffer of pH 3

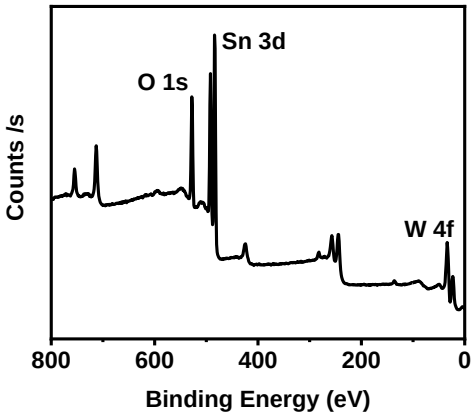


**Figure S1.** XPS survey spectrum of the as-synthesized α-$SnWO_4$, confirming the presence of Sn, W, and O.

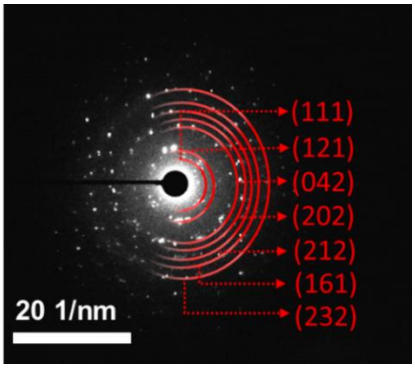


**Figure S2.** Selected area electron diffraction (SAED) pattern of α-$SnWO_4$.

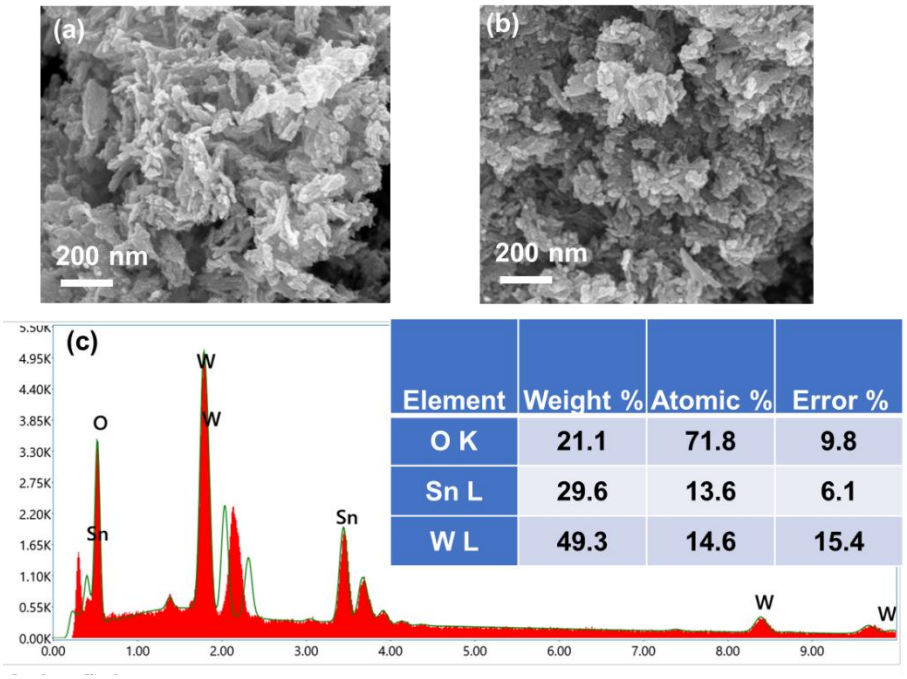


| Element | Weight % | Atomic % | Error % |
|---|---|---|---|
| O K | 21.1 | 71.8 | 9.8 |
| Sn L | 29.6 | 13.6 | 6.1 |
| W L | 49.3 | 14.6 | 15.4 |

**Figure S3.** (a-b) FESEM image of the as-synthesised α-$SnWO_4$. (c) Atomic percentage of Sn, W, and O elements of the area presented in figure 1g.

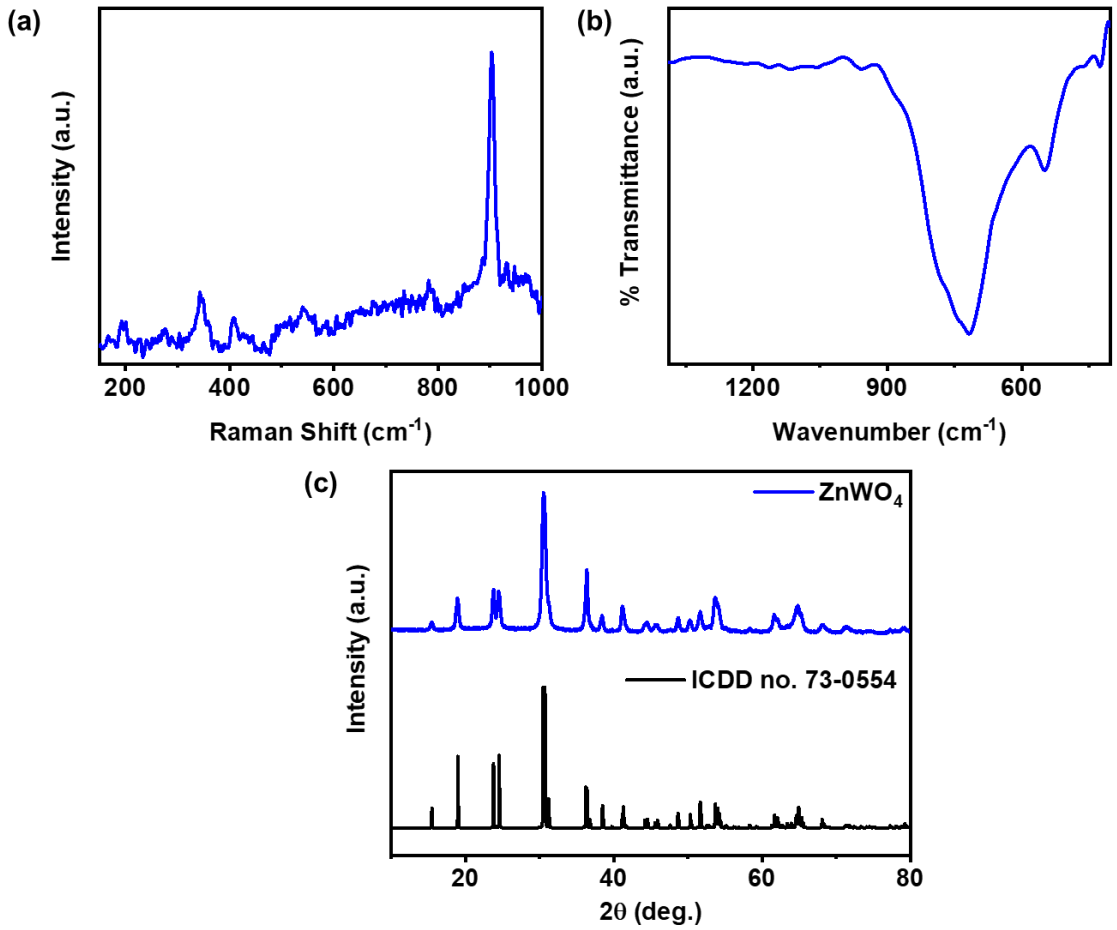


**Figure S4.** (a) Raman, (b) IR, and PXRD pattern along with ICDD data of $ZnWO_4$.

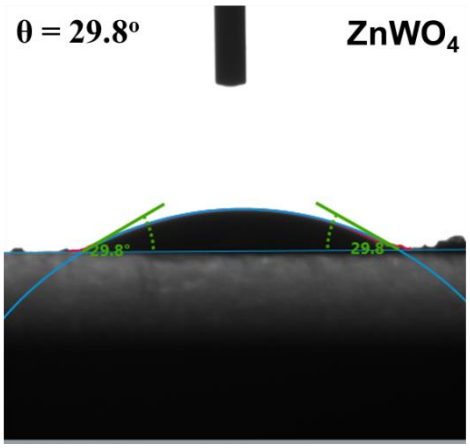


**Figure S5.** Wettability test through contact angle measurement performed with $ZnWO_4$.

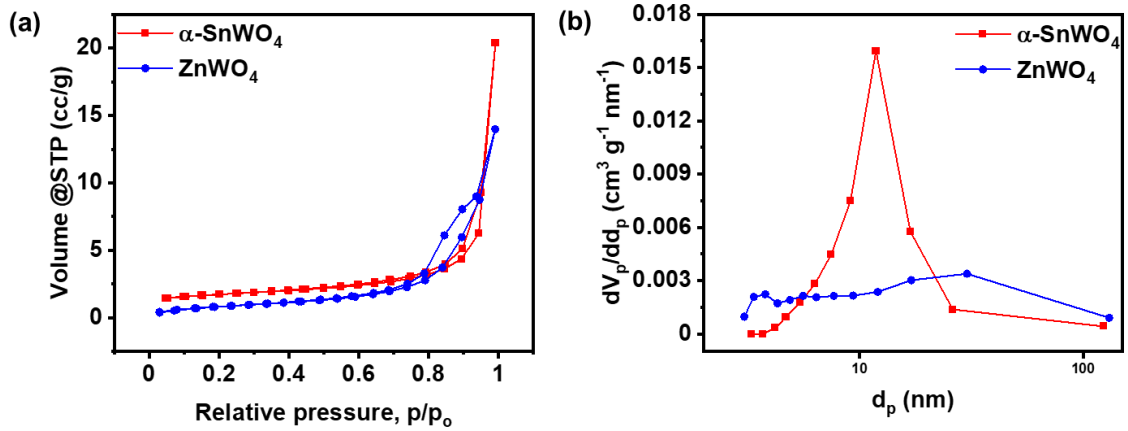


**Figure S6.** $N_2$ adsorption–desorption isotherms obtained for the powder samples; α-$SnWO_4$ (red), and $ZnWO_4$ (blue) and the (b) the pore size distribution obtained from the BET study.

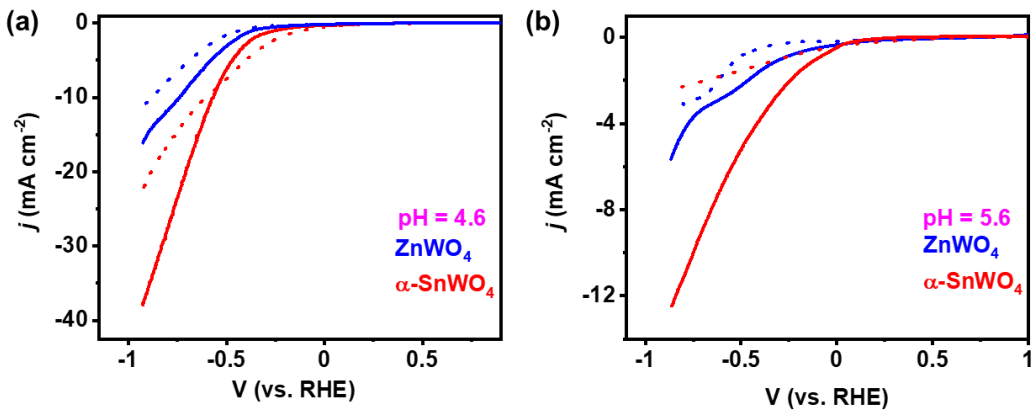


**Figure S7.** Linear sweep voltammograms recorded with $ZnWO_4$ and α-$SnWO_4$ using 0.2 M acetate buffer of (a) pH 4.6, and (b) pH 5.6 without (dotted lines) and with (solid lines) 0.1 M $KNO_3$ using the three-electrode set up (WE: catalyst loaded on CC, RE: Ag/AgCl (aq.) and CE: graphite rod).

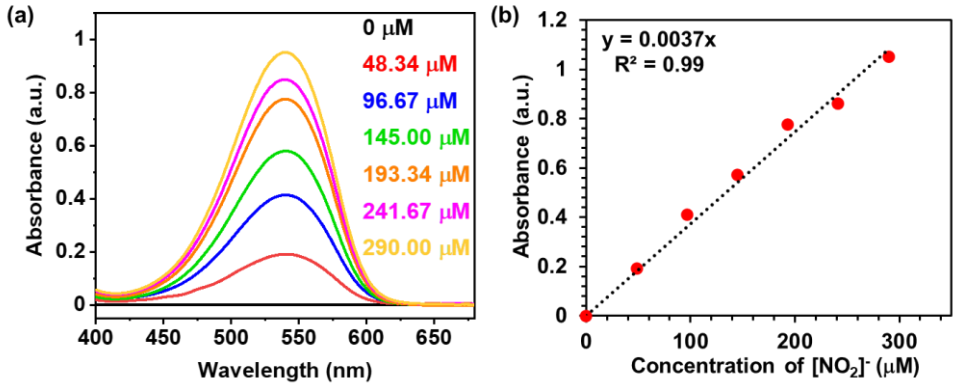


**Figure S8.** Calibration curve for the detection of $[NO_2]^-$ ion through the reported Griess method (see experimental): (a) UV-Vis spectra of standard solution with different concentrations (0 - 290 μM of $[NO_2]^-$), (b) corresponding plot of absorbance at 540 nm versus different concentrations (0 - 290 μM).

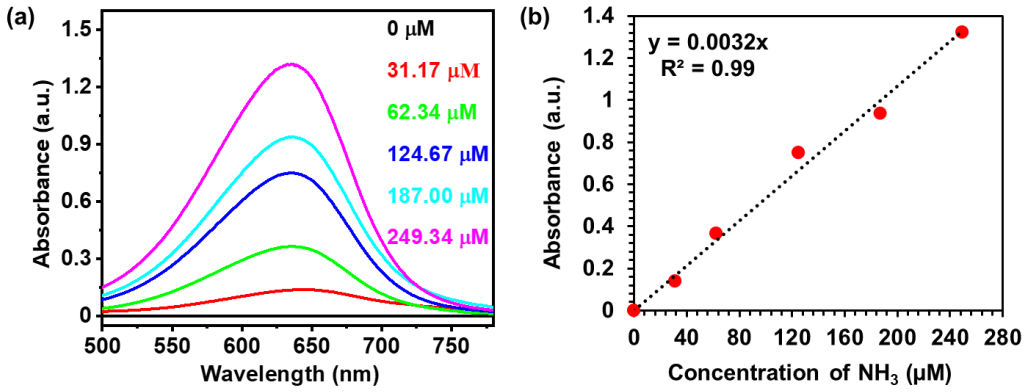


**Figure S9.** Calibration curve for the detection of $NH_3$ ion through the reported Indo-phenol blue method (see experimental); (a) UV-vis spectra of standard solution with different concentrations (0 - 249.34 μM), (b) corresponding plot of absorbance at 640 nm versus different concentrations (0 - 249.34 μM).

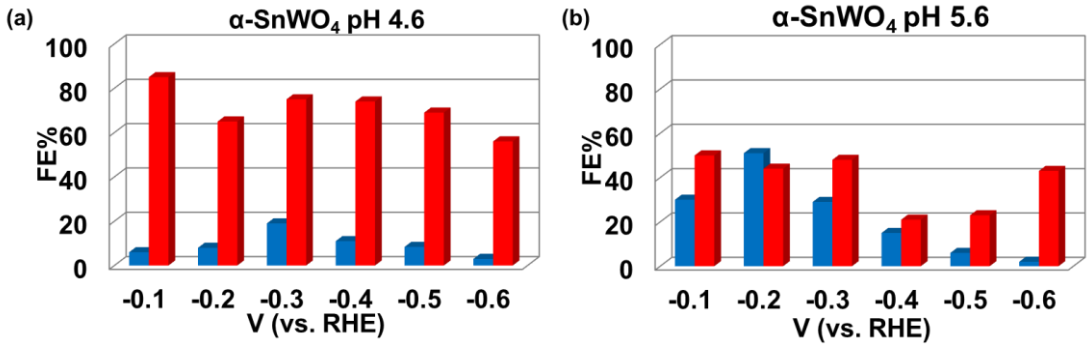


**Figure S10.** FEs for $NH_3$ (red) and $[NO_2]^-$ (blue) production during 1 h chronoamperometric (CA) with α-$SnWO_4$ using 0.1 M $KNO_3$ in acetate buffer (0.2 M) at different applied potentials for pH (a) 4.6, and (b) 5.6.

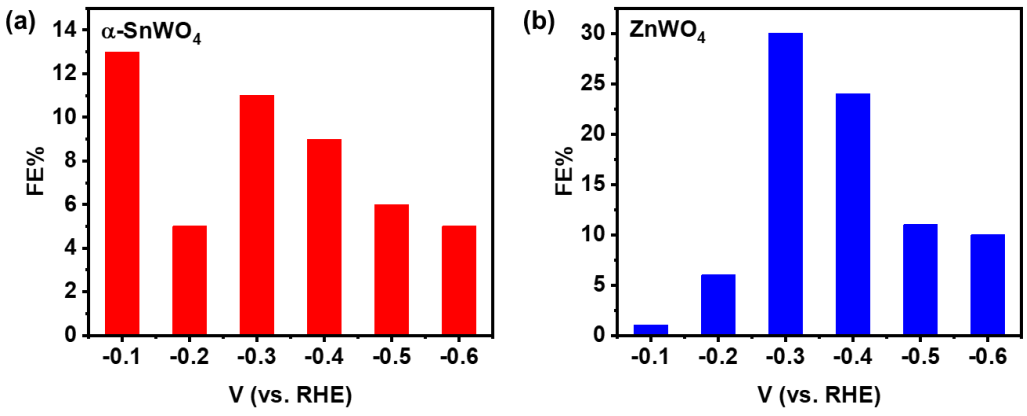


**Figure S11.** FEs for $[NO_2]^-$ production during 1 h chronoamperometric (CA) with (a) α-$SnWO_4$ and (b) $ZnWO_4$ using 0.1 M $KNO_3$ in acetate buffer (0.2 M) at different applied potentials for pH 2.8.

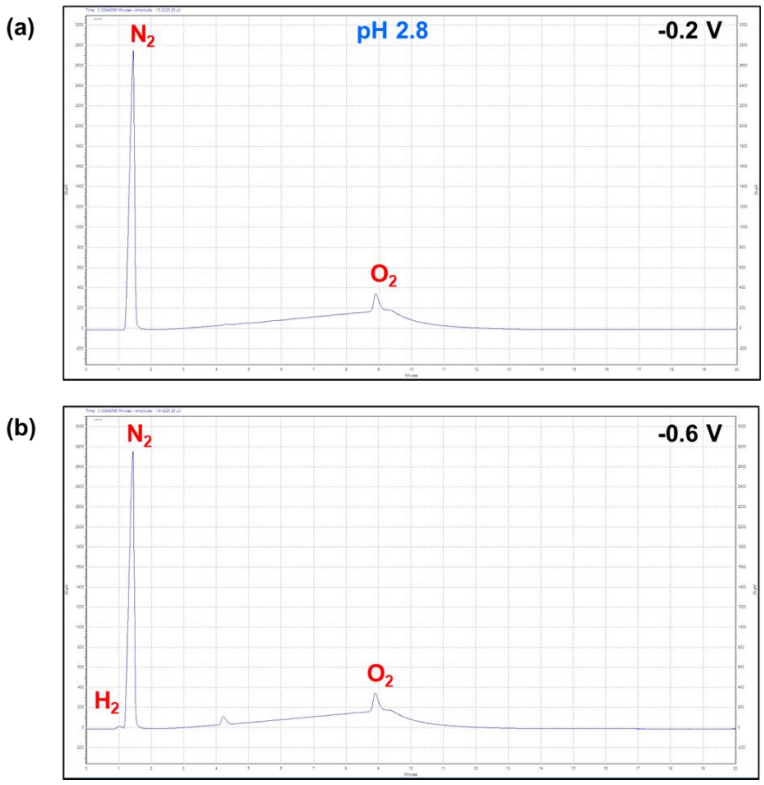


**Figure S12.** GC (TCD) chromatogram obtained for the electrochemical $eNO_3RR$ performed with α-$SnWO_4$ in acetate buffer (0.2 M, pH 2.8) at (a) -0.2 V (b) -0.6 V vs. RHE in a closed container using the three-electrode setup (WE: α-$SnWO_4$ loaded on CC, RE: Ag/AgCl (aq.), and CE: graphite rod).

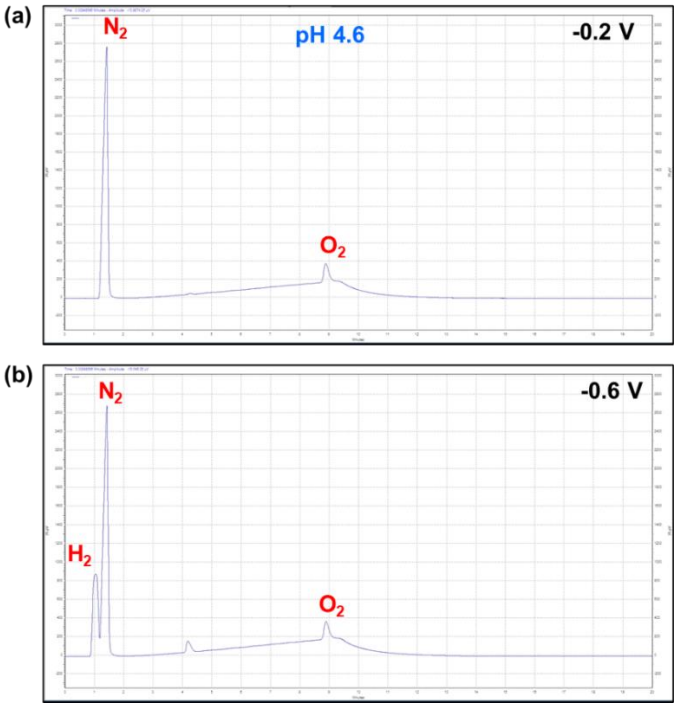


**Figure S13.** GC (TCD) chromatogram obtained for the electrochemical $eNO_3RR$ performed with α-$SnWO_4$ in acetate buffer (0.2 M, pH 4.6) at (a) -0.2 V (b) -0.6 V vs. RHE in a closed container using the three-electrode setup (WE: α-$SnWO_4$ loaded on CC, RE: Ag/AgCl (aq.), and CE: graphite rod).

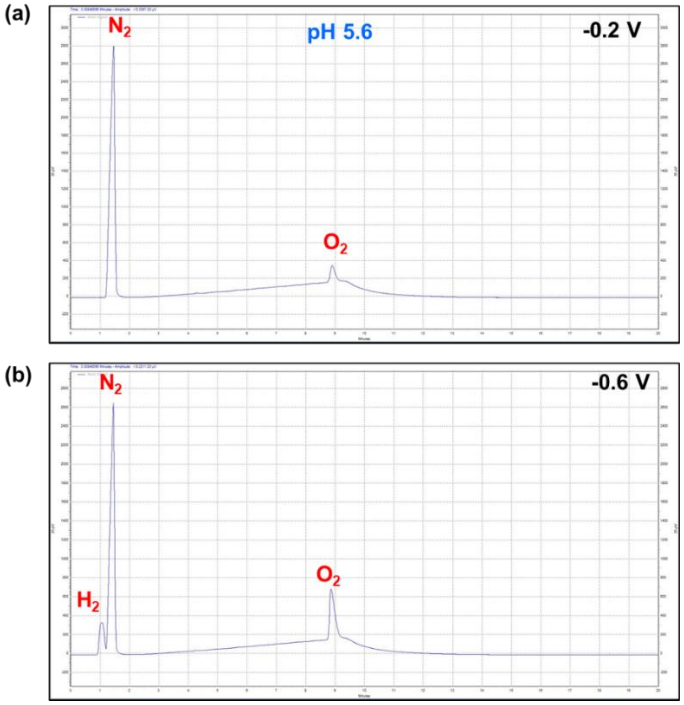


**Figure S14.** GC (TCD) chromatogram obtained for the electrochemical $eNO_3RR$ performed with α-$SnWO_4$ in acetate buffer (0.2 M, pH 5.6) at (a) -0.2 V (b) -0.6 V vs. RHE in a closed container using the three-electrode setup (WE: α-$SnWO_4$ loaded on CC, RE: Ag/AgCl (aq.), and CE: graphite rod).

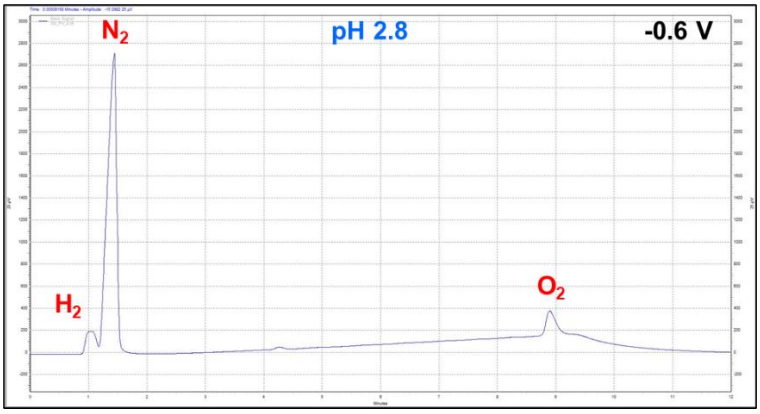


**Figure S15.** GC (TCD) chromatogram obtained for the electrochemical $eNO_3RR$ performed with $ZnWO_4$ in acetate buffer (0.2 M, pH 2.8) at -0.6 V vs. RHE in a closed container using the three-electrode setup (WE: α-$SnWO_4$ loaded on CC, RE: Ag/AgCl (aq.), and CE: graphite rod).

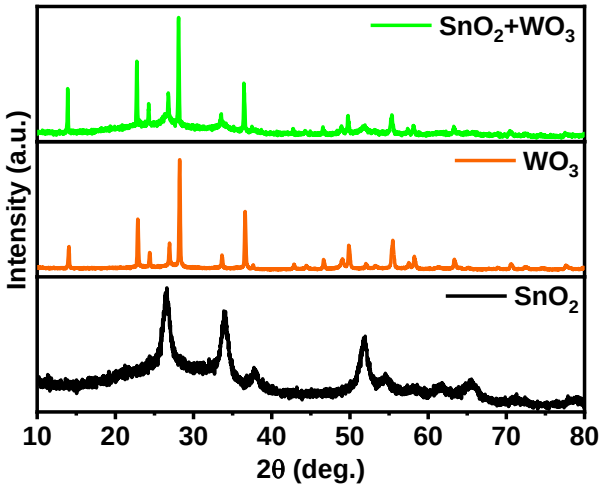


**Figure S16.** PXRD pattern of $SnO_2$ (black), $WO_3$ (orange) and physical mixture (1:1 weight ratio) of $SnO_2$ and $WO_3$ (green).

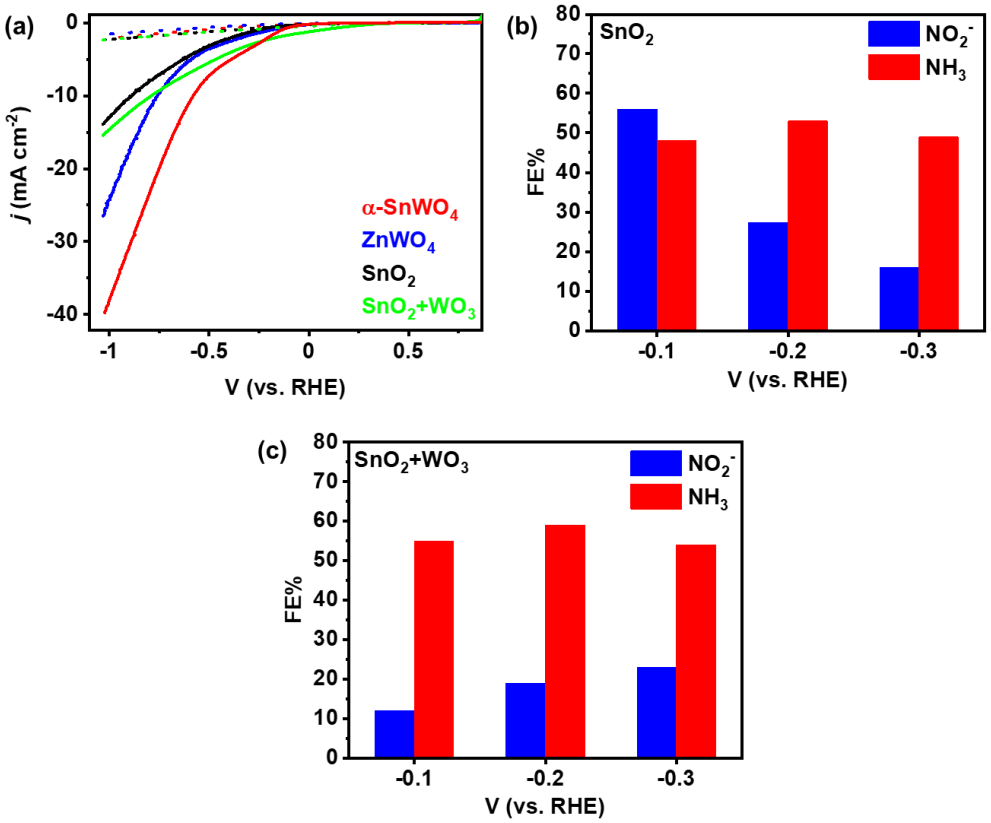


**Figure S17.** (a) Comparison of LSV curves obtained for different materials ($SnWO_4$, $ZnWO_4$, $SnO_2$ and a physical mixture of $SnO_2$+$WO_3$) in acetate buffer (0.2 M, pH 2.8) (dotted lines represent without $KNO_3$ and solid lines represent with 0.1 M $KNO_3$). FEs of $[NO_2]^-$ and $NH_3$ produced during e$NO_3$RR with (b) $SnO_2$, (c) a physical mixture of $SnO_2$+$WO_3$.

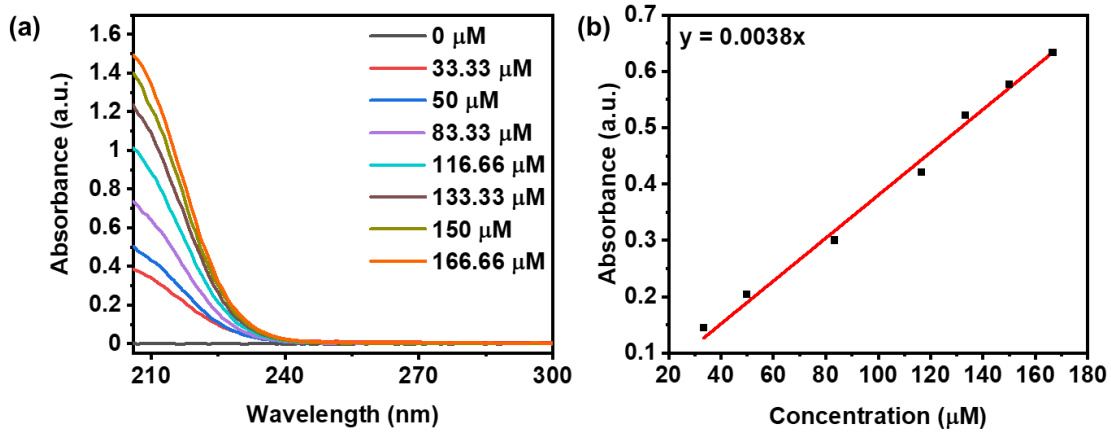


**Figure S18.** Calibration curve for the detection of $NO_3^-$ ion (see experimental); (a) UV-vis spectra of standard solution with different concentrations (0 - 166.66 μM), (b) corresponding plot of absorbance at 220 nm versus different concentrations (0 - 166.66 μM).

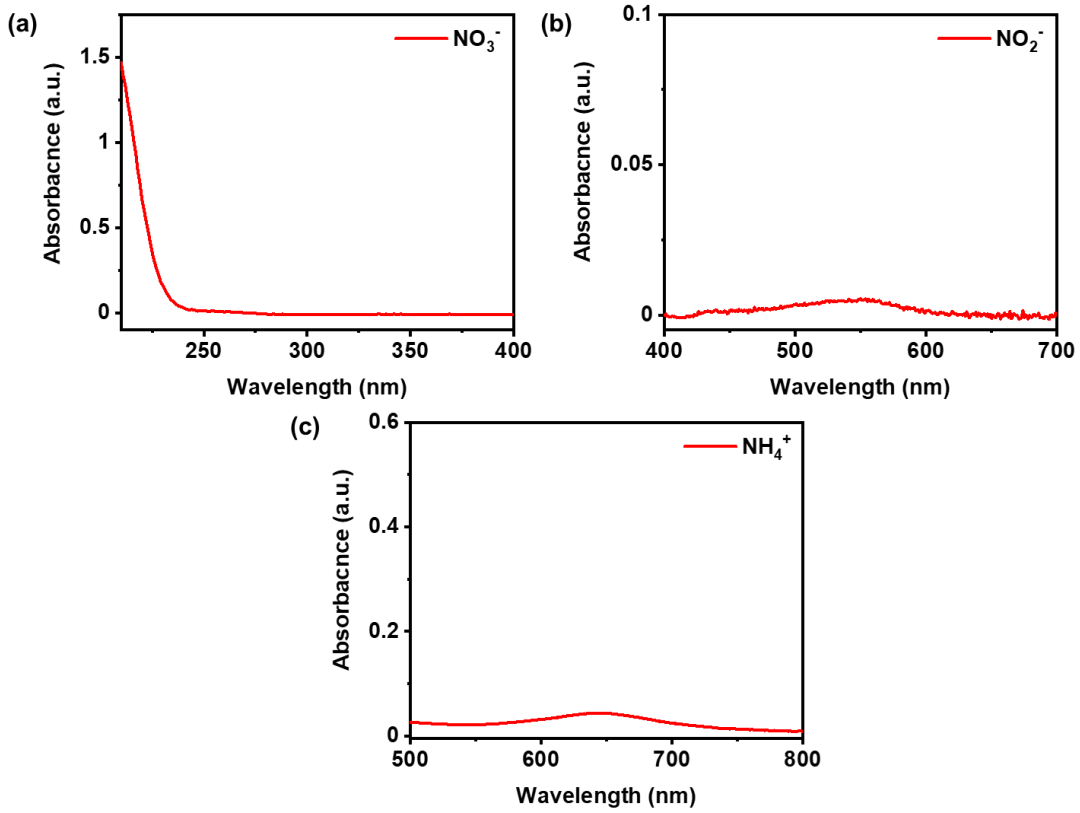


**Figure S19.** UV-vis spectra of tapwater containing ions: (a) $NO_3^-$, (b) $NO_2^-$, and (c) $NH_4^+$.

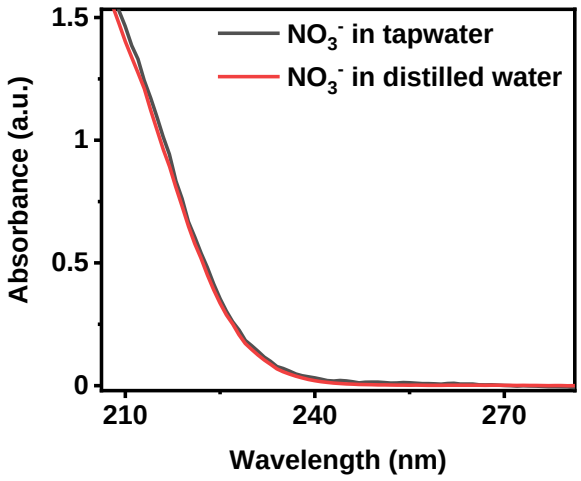


**Figure S20.** Comparison of UV-vis spectra of $NO_3^-$ ions present in tapwater (grey curve) and 11.1 mg $L^{-1}$ of $KNO_3$ added in distilled water (red curve).

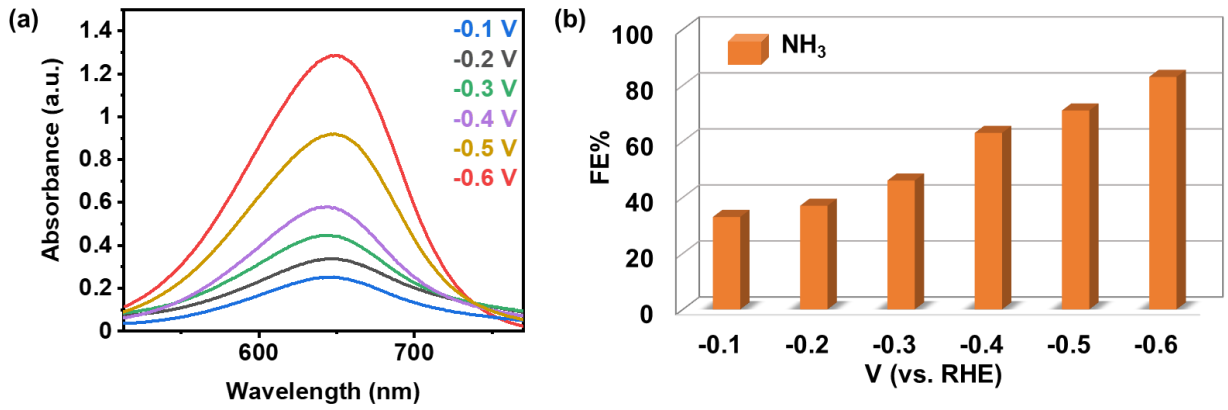


**Figure S21.** (a) UV-Vis spectra, and (b) comparison of FE% of $NH_3$ obtained after CA at different potentials in acetate buffer made in tapwater (0.2 M, pH 3).

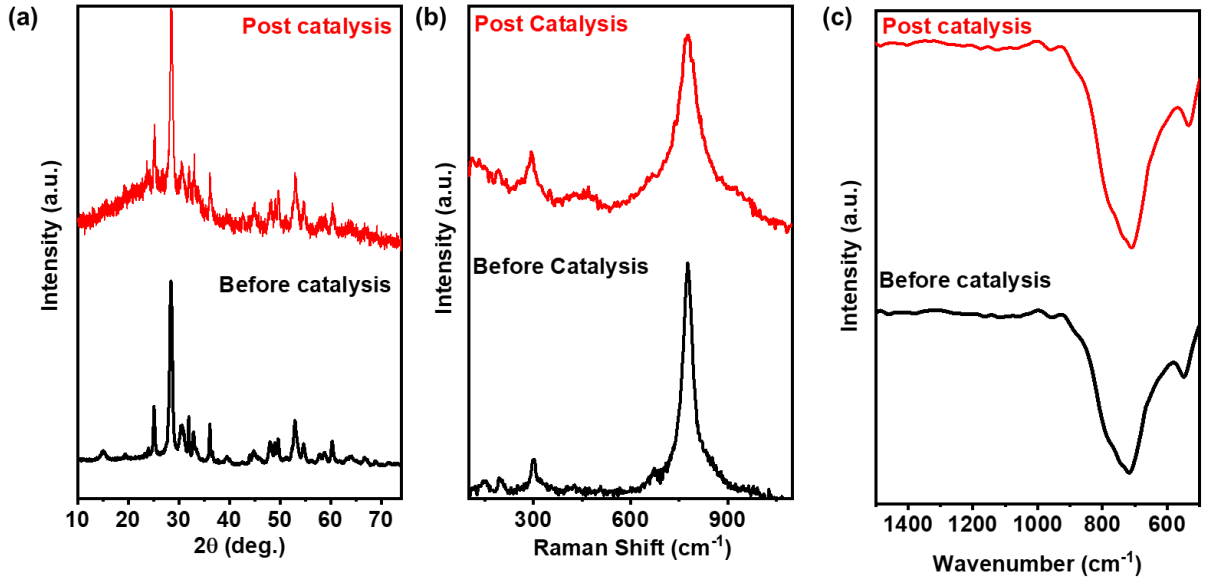


**Figure S22.** (a) PXRD pattern, (b) Raman spectra, and (c) FTIR spectra of used α-$SnWO_4$/CC electrode or the extracted material from the electrode after e$NO_3$RR. (Black curves are the spectra of as-synthesized materials.

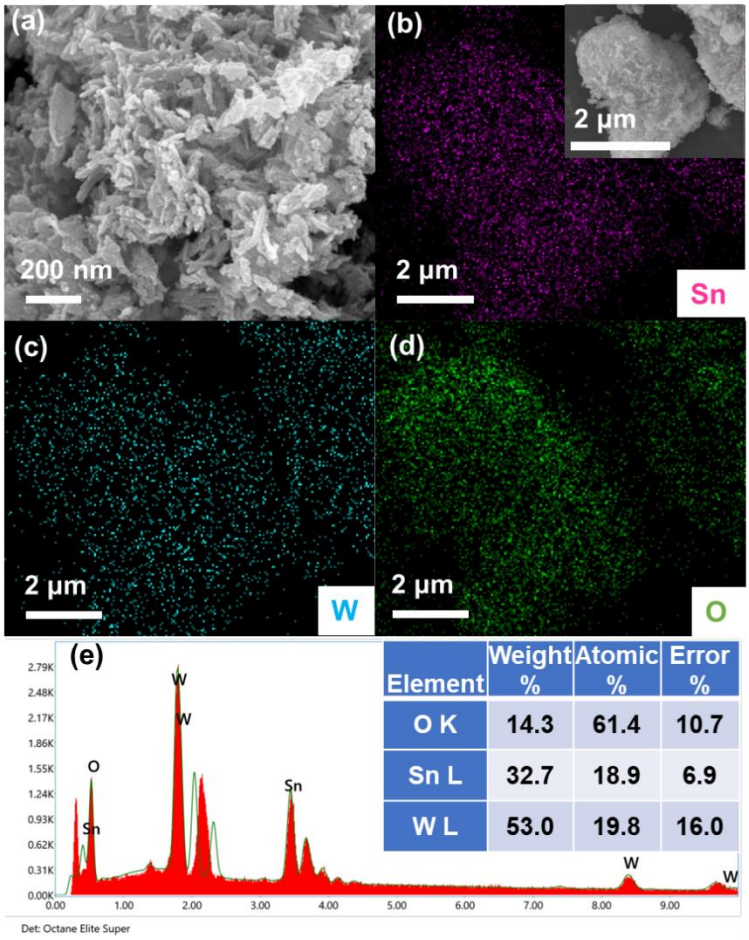


| Element | Weight % | Atomic % | Error % |
|---|---|---|---|
| O K | 14.3 | 61.4 | 10.7 |
| Sn L | 32.7 | 18.9 | 6.9 |
| W L | 53.0 | 19.8 | 16.0 |

**Figure S23.** (a) FESEM image of α-$SnWO_4$, (b-d) FESEM–EDX elemental mapping of corresponding elements, such as (b) Sn, (c) W, and (d) O elements present on area (b: inset). (e) atomic percentage of Sn, W, and O elements after e$NO_3$RR.

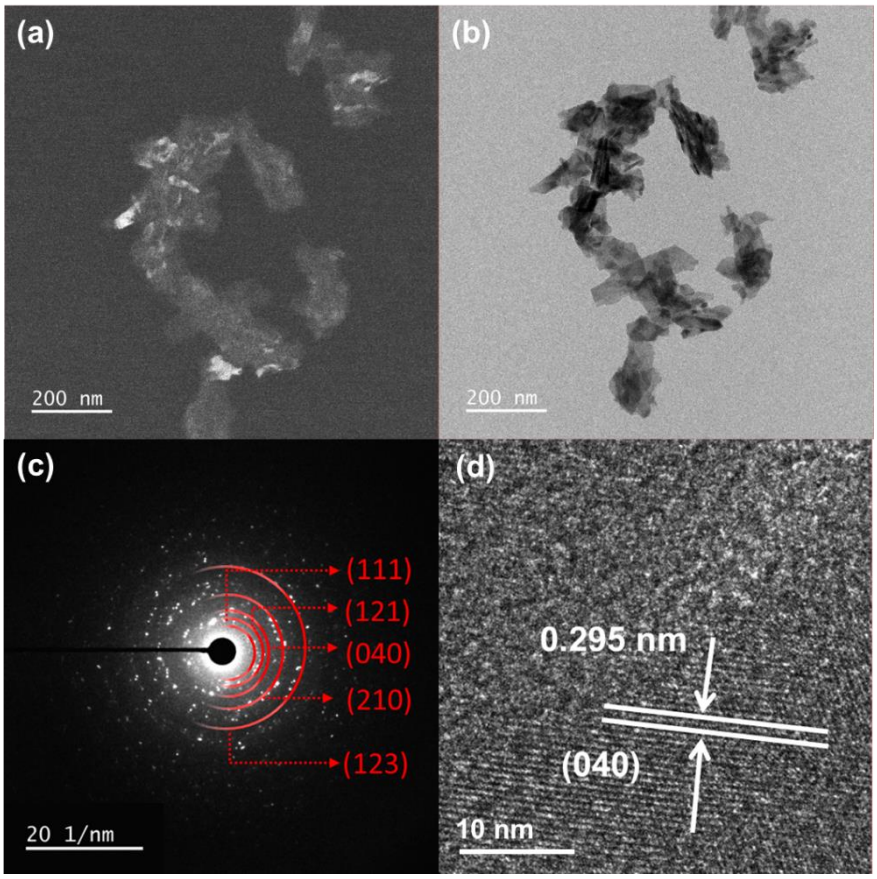


**Figure S24.** (a) Brightfield TEM image of α-$SnWO_4$. (b) Darkfield TEM image obtained by selectively illuminating the particles with (040) facets, (c) selected area electron diffraction (SAED) pattern of the particles of α-$SnWO_4$, and (d) HRTEM image of α-$SnWO_4$ with lattice fringes for (040) planes with 0.295 nm interplanar distance after e$NO_3$RR.

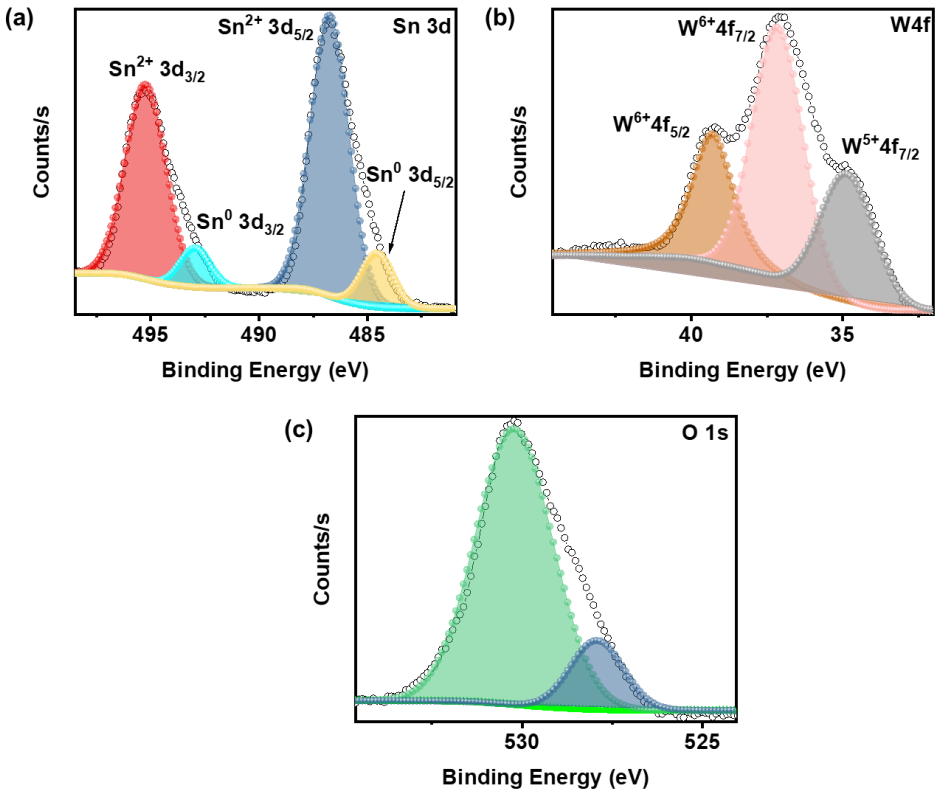


**Figure S25**. Core-level Sn 3d, W 4f and O 1s XPS spectra recorded with the material isolated from the used α-$SnWO_4$/CC electrode after e$NO_3$RR.

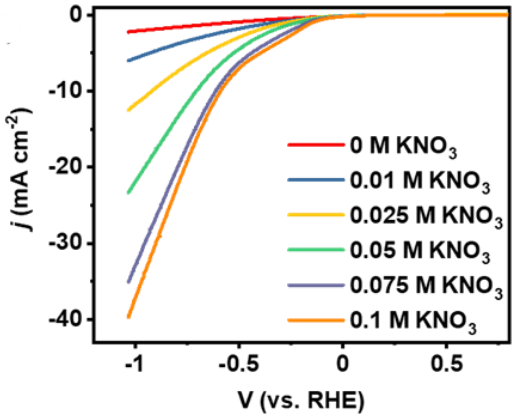


**Figure S26.** LSV curves recorded in different concentrations of $KNO_3$ (0.01–0.1 M) with α-$SnWO_4$ as the electrocatalyst.

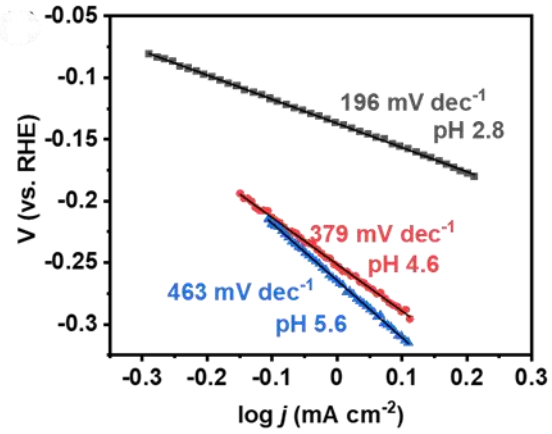


**Figure S27.** Tafel slopes obtained from the LSV scans recorded with α-$SnWO_4$/CC electrode in the acetate buffer of various pH (2.8, 4.6, and 5.6).

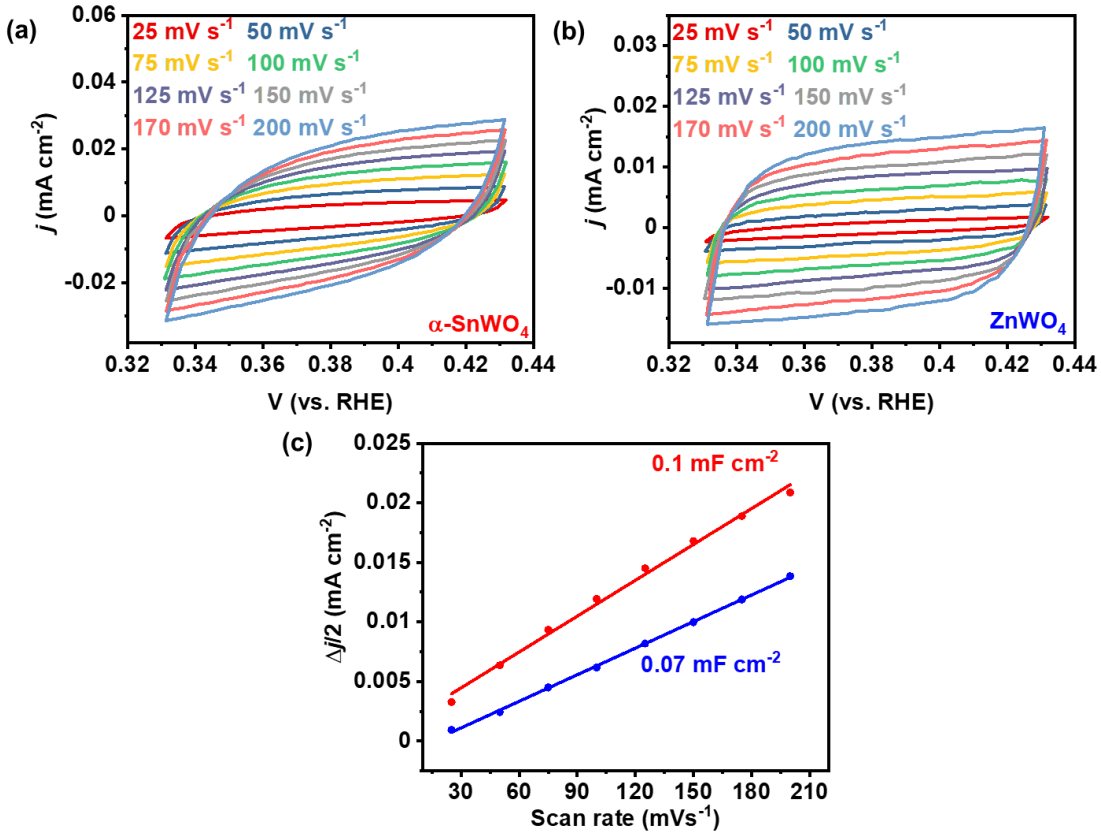


**Figure S28.** Cyclic voltammograms recorded with (a) α-$SnWO_4$ and (b) $ZnWO_4$ (in the non-Faradic region at different scan rates (25 mV $s^{-1}$ to 200 mV $s^{-1}$) in acetate buffer (pH 3, 0.2 M) using the three-electrode set up (WE: catalyst loaded on C cloth RE: Ag/AgCl (aq.) and CE: graphite rod). (c) Comparison of $C_{dl}$ for α-$SnWO_4$ (red) and $ZnWO_4$ (blue).

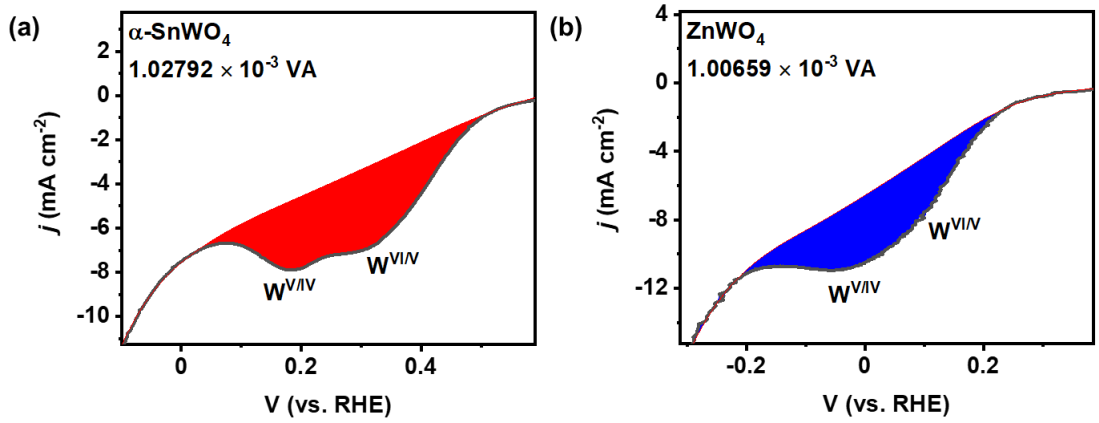


**Figure S29.** The redox region from the CV cycle (Figure 2b) showing the surface area for the peaks corresponding to the reduction of $W^{VI}$.

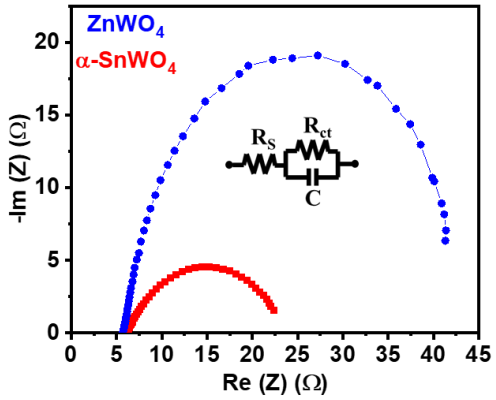


**Figure S30.** Nyquist plots (from the impedance study) obtained for $ZnWO_4$ and α-$SnWO_4$ in acetate buffer (0.2 M, pH 2.8) at -0.6 V vs. RHE (inset: equivalent circuit fitting).

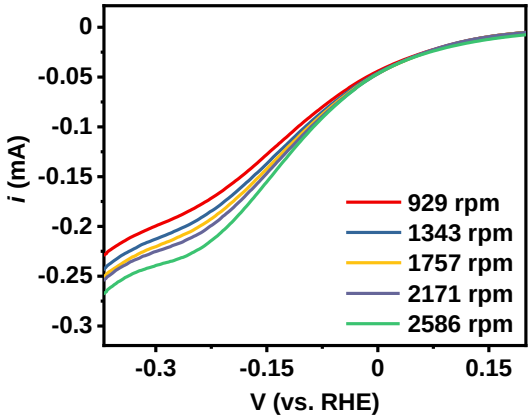


**Figure S31.** Rotating rate-dependent LSV curves (disc current) with α-$SnWO_4$ deposited on the disk of the RDE working electrode.

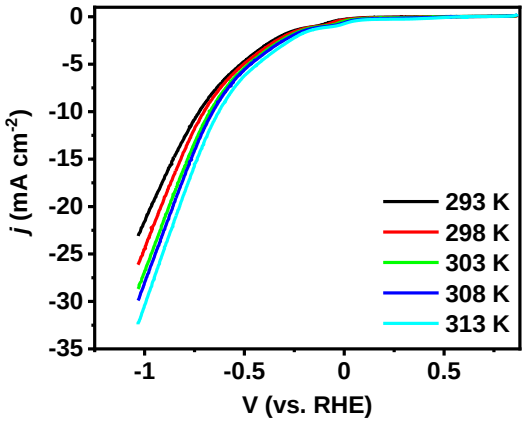


**Figure S32.** Linear sweep voltammograms recorded at different temperatures (293 K to 313 K) with α-$SnWO_4$/CC electrode under the above mentioned e$NO_3$RR conditions.

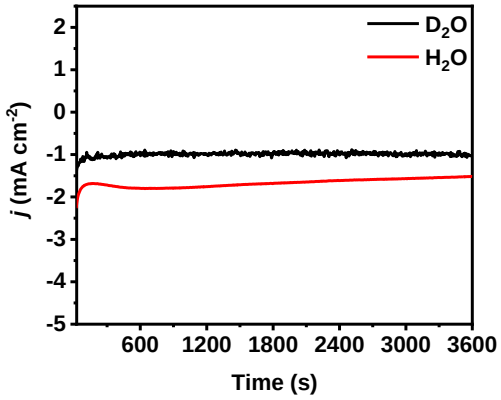


**Figure S33.** Chronoamperometry (CA) studies carried out with α-$SnWO_4$ using $H_2O$, and $D_2O$ as an electrolyte solvent to make acetate buffer (0.2 M, pH 2.8) with 0.1 M $KNO_3$ under the three-electrode setup (WE: α-$SnWO_4$ loaded on C cloth RE: Ag/AgCl (aq.) and CE: graphite rod).

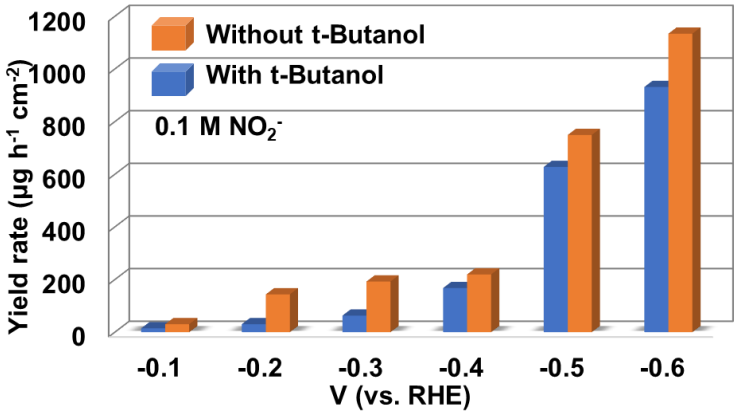


**Figure S34.** Yield rate for $NH_3$ produced during 1 h chronoamperometric (CA) with α-$SnWO_4$ using 0.1 M $NO_2^-$ in acetate buffer (0.2 M, pH 2.8) at different applied potentials in absence of butanol (orange) and in presence of butanol (blue).

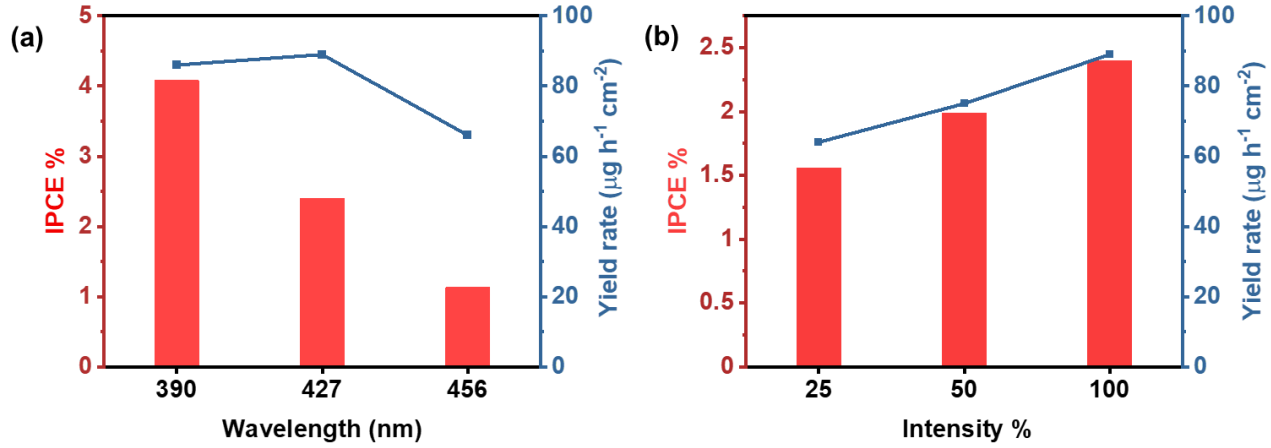


**Figure S35.** (a) Comparison of IPCE% and yield rate of $NH_3$ for α-$SnWO_4$ at 390, 427, and 456 nm wavelength. (b) Comparison of IPCE% and yield rate of $NH_3$ for α-$SnWO_4$ at 427 nm (137 mW $cm^{-2}$) with different intensities of the power density (25%, 50% and 100%).

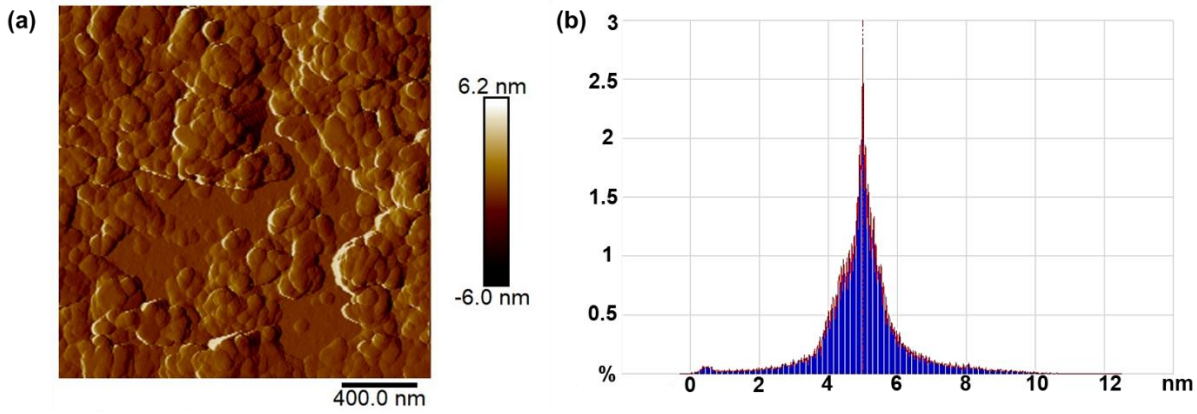


**Figure S36.** (a) Atomic force microscopy (AFM) images a selected region of $SnWO_4$ particles and corresponding (b) depth profile obtained from the area indicated in (a).

## References:


1. H. K. Basak, M. K. Adak, A. Rajput and B. Chakraborty, *ACS Appl. Mater. Interfaces*, 2025, **17**, 9391-9406.
2. H. Qiu, Q. Chen, J. Zhang, X. An, Q. Liu, L. Xie, W. Yao, X. Sun and Q. Kong, *Inorg. Chem. Front.*, 2023, **10**, 3909-3915.
3. X. Bai, K. Zhou, L. Lin, H. Li, Q. Li and G. Fan, *Fuel*, 2024, **376**, 132746.
4. Q. Gong, H. Zhao, W.-D. Zhang, J.-D. Feng, Y. Zhang, Y. Zhang, J. Liu, B. Liu, J. Zhang, X. Yang, J. Wang and X. Yan, *Chem. Eng. J.*, 2025, **504**, 158819.
5. Z. Xue, C. Sun, M. Zhao, Y. Cui, Y. Qu, H. Ma, Z. Wang and Q. Jiang, *ACS Appl. Mater. Interfaces*, 2021, **13**, 59834-59842.
6. R. Qi, Q. Jiang, M. Zhong, W. Li, S. Ren, Y. Wang, M. Feng and X. Lu, *Chem. Eng. J.*, 2024, **496**, 154094.
7. L. Wang, H.-N. Liu, X. Meng, C.-H. Sun, H.-D. Liu, L.-Y. Gong, Z.-H. Yan and J. Wang, *Rare Met.*, 2024, **43**, 2851-2858.
8. Y. Ran, T. Li, C. Zhong, Y. Wang, C. Li and W. Hu, *J. Alloys Compd.*, 2025, **1026**, 180522.
9. G. Zhang, F. Wang, K. Chen, J. Kang and K. Chu, *Adv. Funct. Mater.*, 2024, **34**, 2305372.
10. S. Gautam, A. Kundu, L. Mallick and B. Chakraborty, *J. Mater. Chem. A*, 2025, **13**, 41972-41985.
11. L. Mallick, H. V. Annadata and B. Chakraborty, *ACS Appl. Mater. Interfaces*, 2024, **16**, 32385-32393.